PAPER

Vapor–liquid assisted chemical vapor deposition of $\operatorname{Cu}_2\operatorname{X}$ materials

To cite this article: M Arslan Shehzad et al 2022 2D Mater. 9 045013

View the article online for updates and enhancements.

You may also like

- <u>Characterization of InMnSb epitaxial films</u> <u>for spintronics</u>
 L Lari, S Lea, C Feeser et al.
- Incorporation of the electrode–electrolyte interface into finite-element models of metal microelectrodes

Donald R Cantrell, Samsoon Inayat, Allen Taflove et al.

- Thermal gelation and tissue adhesion of biomimetic hydrogels Sean A Burke, Marsha Ritter-Jones, Bruce P Lee et al.

2D Materials



RECEIVED 16 May 2022

REVISED

11 July 2022

ACCEPTED FOR PUBLICATION 25 July 2022

PUBLISHED
4 August 2022

PAPER

Vapor-liquid assisted chemical vapor deposition of Cu₂X materials

M Arslan Shehzad^{1,3,9}, Yea-Shine Lee^{1,9}, Matthew Cheng¹, Dmitry Lebedev¹, Alexander C Tyner⁵, Paul Masih Das¹, Zhangyuan Gao¹, Pallab Goswami^{2,5}, Roberto dos Reis^{1,3}, Mark C Hersam^{1,6,7}, Xinqi Chen^{3,8,*} and Vinayak P Dravid^{1,3,4,*}

- Department of Material Science and Engineering, Northwestern University, Evanston, IL 60208, United States of America
- Department of Physics, Northwestern University, Evanston, IL 60208, United States of America
- Northwestern University Atomic and Nanoscale Characterization Experimental (NUANCE) Center, Northwestern University, Evanston, IL 60208, United States of America
- International Institute for Nanotechnology (IIN), Northwestern University, Evanston, IL 60208, United States of America
- ⁵ Graduate Program in Applied Physics, Northwestern University, Evanston, IL 60208, United States of America
- Department of Chemistry, Northwestern University, Evanston, IL 60208, United States of America
- Department of Electrical and Computer Engineering, Northwestern University, Evanston, IL 60208, United States of America
- ⁸ Department of Mechanical Engineering, Northwestern University, Evanston, IL 60208, United States of America
- ⁹ Equal contributing authors.
- * Authors to whom any correspondence should be addressed.

E-mail: xchen@northwestern.edu and v-dravid@northwestern.edu

Keywords: vapor-liquid CVD, Cu2X, Cu2Te, metal-semiconductor transition

Supplementary material for this article is available online

Abstract

Transition metal dichalcogenides (TMDs) are known for their layered structure and tunable functional properties. However, a unified understanding on other transition metal chalcogenides (i.e. M_2X) is still lacking. Here, the relatively new class of copper-based chalcogenides Cu_2X (X = Te, Se, S) is thoroughly reported. Cu_2X are synthesized by an unusual vapor–liquid assisted growth on a $Al_2O_3/Cu/W$ stack. Liquid copper plays a significant role in synthesizing these layered systems, and sapphire assists with lateral growth and exfoliation. Similar to traditional TMDs, thickness dependent phonon signatures are observed, and high-resolution atomic images reveal the single phase Cu_2 Te that prefers to grow in lattice-matched layers. Charge transport measurements indicate a metallic nature at room temperature with a transition to a semiconducting nature at low temperatures accompanied by a phase transition, in agreement with band structure calculations. These findings establish a fundamental understanding and thrust Cu_2 Te as a flexible candidate for wide applications from photovoltaics and sensors to nanoelectronics.

1. Introduction

Recently, large area growths via chemical vapor deposition (CVD) of two-dimensional (2D) transition metal dichalcogenides (TMDs) on different substrates [1] have opened avenues to implement them in practical applications [2]. However, while highly effective for growing certain TMDs, CVD is still limited in terms of controlling the crystal morphology, orientation, and chemical composition. The development of alternative synthesis methods has the potential to enable large area growths of other low-dimensional materials [3].

In general, CVD requires a vapor precursor that interacts with a substrate surface via nucleation and diffusion, yielding layered crystals such as TMDs [4]

and graphene [5]. In contrast, Xu et al has recently used a liquid-based catalyst to enable diffusion-based large area growth of MXene's [6]. This same group used a similar approach to successfully synthesize novel MoSi₂N₄ (MAX) materials [7]. We extended this method to better understand the growth mechanism of MXene's [8]. This approach is similar to the vapor-liquid-solid (VLS) mechanism where the precipitation of a supersaturated catalyst yields 1D nanostructures [9], where the liquid catalyst is only used for diffusion of metal precursors. Recent work on growths of metal oxides on liquid metal surfaces [10] and monolayer MoSe₂ [11] on molten glass further demonstrates the potential of liquid-mediated synthesis techniques to enable large area growths of emerging layered structures.

Cu-based chalcogenides (Cu₂X) have recently garnered significant attention for their potential in thermoelectrics and photovoltaic applications [12–15]. In particular, the three-dimensional (3D) Cu₂Te is expected to surpass the thermoelectric performance of Cu₂Se and Cu₂S due to the relatively low electronegativity and high atomic number of tellurium [13]. However, small variations in synthesis methods yield different stable and metastable copper tellurides, complicating the precise identification of the crystal structure [13, 16–18].

Reports on the 2D layered form of copper telluride have recently expanded upon the active work on 3D copper telluride. A study has reported the versatility of Cu₂Te, where one phase can display metallic characteristics [19] while another can display semiconductor characteristics with minor atomic structural differences [17]. Atomically sharp metalsemiconductor interfaces for application in electronic devices can thus be achieved. The tendency of Cu to be sandwiched between chalcogens also contributes to air-stability, which makes Cu₂Te a promising candidate for ultrathin channel FET devices [12]. A temperature-dependent reversible phase transformation of Cu₂Te from P3m1 to P6/mmm phase has also been reported [20]. However, the 2D copper telluride also faces challenges of stoichiometric synthesis and structure identification despite promising opportunities offered by its layered nature. Various efforts have been made to stabilize the stoichiometric Cu₂Te such as spark plasma sintering [21], molecular beam epitaxy on bilayer graphene-SiC(0001) [22] or Cu(111) [23], and VLS growth [17]. Despite these efforts, the capability to controllably isolate a single phase of Cu₂Te remains limited [17].

In this work, we report a vapor-liquid assisted CVD method for reliably synthesizing and exfoliating a P3m1 hexagonal, 2D layered Cu2Te. We show this growth scheme is extendable to other Cu₂X (X = Se, S) materials. We demonstrate that sapphire above the Cu foil plays a critical role in promoting not only lateral growth, but also exfoliation to fewlayers and transfer to other substrates such as traditional silicon wafers. We also report the evolving phonon modes from bulk to few-layer 2D Cu₂Te and detail the atomic structure with scanning transmission electron microscopy (S/TEM). Charge transport measurements and density functional theory (DFT) band structure calculations both point towards the metallic nature of P3m1 Cu₂Te at room temperature, with a transformation to a semiconducting phase at low temperatures. Although exciting electronic properties of 2D tellurides such as controllable phase or bandgap in MoTe₂ and reduced thermal conductivity in thermoelectric Bi₂Te₃ have been reported, reports on temperature dependent electronic property are limited. In this aspect, Cu₂Te has a wide application potential offering flexible tunability from metallic to semiconducting state with a concurrent structural transformation [24].

2. Results and discussion

A stack of $Al_2O_3/Cu/W$ is used to grow crystals of the Cu_2X system by melted catalyst-based CVD (refer to section 4 for details). Different chalcogen powders (S, Se, Te) are placed 15 cm away from the center of the tube to reach the vaporization temperature, and a mix of Ar/H_2 gas carries the vaporized chalcogen to the molten Cu catalyst surface at the center of the tube. Figure 1(a) shows the schematics of the growth scheme. First, the temperature is ramped above the melting temperature of Cu before it is dropped to $1080\,^{\circ}$ C for growth. Growth is held for different durations ($T_{\rm growth}$) as shown in figure S1. As expected, longer growth times lead to higher density of crystals on the substrate surface.

Melting of the Cu catalyst is an important protocol during the growth as it increases the diffusion coefficients of the chalcogen atoms in Cu [25]. As a result, even when the top surface of the catalyst is covered with Al_2O_3 , the chalcogen vapors diffuse through the edges of the molten catalyst as shown in figure 1(a). This is supported by the temperature-dependent growth series, which shows no crystal-line growth below the catalyst melting temperature as shown in figure S2.

Furthermore, careful control of the Te concentration was utilized to understand the initial phase of growth. Therefore, the same growth protocol was maintained with a decreased concentration (\sim 10 mg) of Te. After diffusion, nucleation on the Cu catalyst surface in contact with sapphire becomes preferrable both due to hydrogen flow that reduces contamination on the Cu foil and the epitaxy offered by the sapphire as outlined in figure S3(a). Next, growth occurs during the temperature ramp down process on the surface of Cu in contact with sapphire, and a mix of triangular and round crystal edges can be observed as shown in the optical image in figure 1(a). Although the triangular geometry is thermodynamically favorable, the abundance of precursor Cu and high reaction temperature may push to a kinetically controlled rapid growth, leading to some round crystal edges [26, 27]. Random, non-uniform distribution of crystals throughout the copper surface suggests saturation via the molten catalyst. The new small crystals often merge with pre-existing crystals through edge site reactivity, and increase in size as shown in the magnified optical image in figure 1(a) [28]. Multilayer growth continues during the cooling process, where the remaining precursors adsorb on the formed crystal surface rather than diffuse to the edges, as diffusion would energetically require high temperatures [28]. These optical images, where Cu₂Te is in green

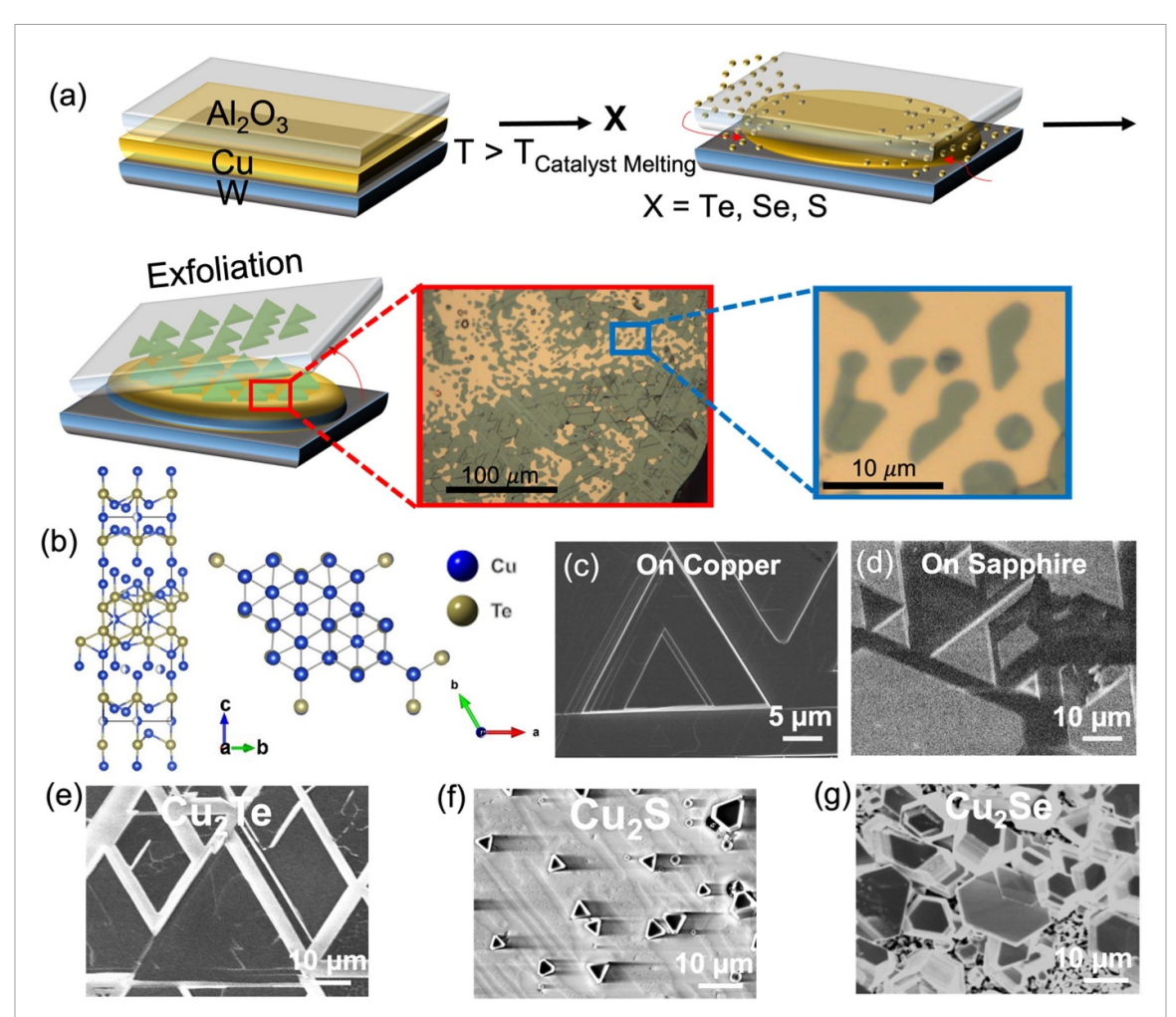


Figure 1. Growth scheme of Cu_2X systems: schematic of the growth of Cu_2X materials using a W/Cu/Al₂O₃ sandwich is shown in (a). Melting of the catalyst is essential to diffuse the incoming vapor species (X = Te, Se, Se) to form Cu_2X . Nucleation and growth occurs on the Cu surface in contact with sapphire, and early growth crystals in the magnified optical image show both triangular and round edges. Exfoliation is done by peeling off the sapphire substrate. The atomic structure of Cu_2X is shown in (b). SEM images of Cu_2X is no copper and sapphire substrates are shown in (c) and (d), respectively. SEM images in (e) and (f) show representative Cu_2X (X = Te, Se) grown on sapphire.

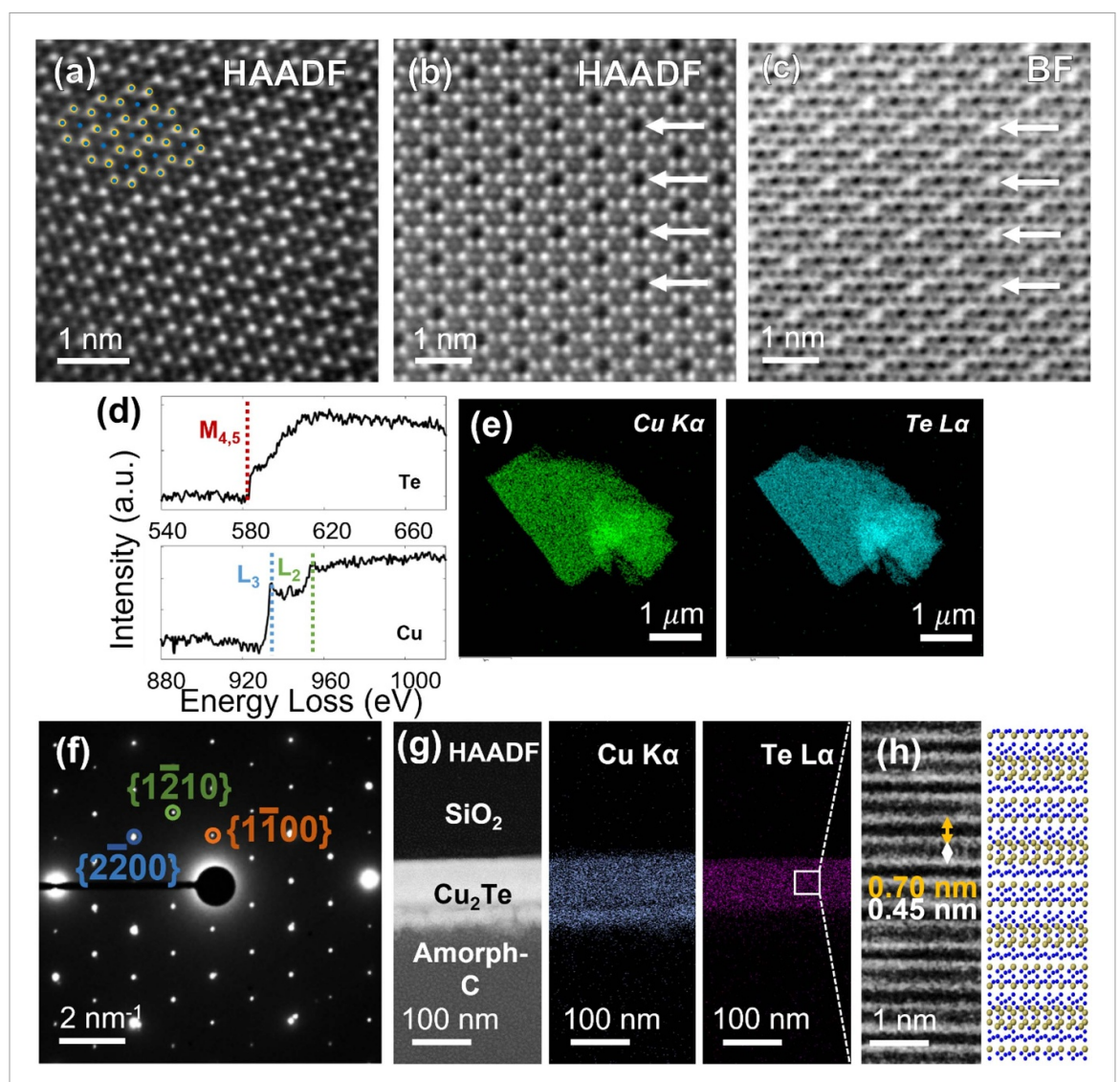
and Cu is in yellow, also demonstrate that the base of the molten Cu often remains unreacted as there is excess Cu.

Figure 1(b) shows the schematics of the atomic structure of P3m1 2D Cu₂Te crystals. Figures 1(c) and (d) show SEM images of crystals grown on Cu and sapphire surfaces, respectively. The growth on sapphire enables facile exfoliation from bulk to fewlayers by simply peeling off after the reaction is complete. Large areas of crystals grown on sapphire are shown in figure S3. Thicker crystals adjacent to thinner ones confirm the exfoliation on sapphire. Triangular islands and edges indicate the hexagonal and layered nature of the grown crystals. Different structures, most of them triangular, are shown in figure S4. Extension to other Cu₂X materials (Cu₂Se, Cu₂S) is shown in figures 1(e)-(g), which highlights the versatility of this growth mechanism for related material systems. The elemental and structural composition of these crystals are confirmed using energy dispersive x-ray spectroscopy (EDS) and x-ray photoelectron spectroscopy (XPS) as shown in figure S5.

To characterize the atomic structure of the grown crystals and gain more insight into the growth mechanism, TEM samples are prepared by wetting the sapphire growth substrate with ethanol, then gently swiping with a molybdenum lacey carbon TEM grid. The presence of Cu and Te is observed with electron energy loss spectroscopy (EELS) and EDS on a bulk crystal as shown in figures 2(d) and (e). The selected area electron diffraction (SAED) pattern of a fewlayer Cu₂Te flake shown in figure 2(f) further highlights the single phase, crystalline products of our synthesis technique. This pattern is closely aligned to the [0001] zone axis of the hexagonal crystal structure. Diffraction spots from three family of planes, $(1\bar{1}00)$, $(1\bar{2}10)$, $(2\bar{2}00)$, are indexed in orange, green, and blue, respectively.

The in-plane atomic structure is shown in the high-resolution STEM high angle annular dark field (HRSTEM-HAADF) image of figure 2(a). The central column of Cu atoms appears dimmer relative to the surrounding six columns of mixed Cu and heavier Te atoms. The distance between the closest bright

2D Mater. 9 (2022) 045013 M A Shehzad et al



spots is 0.26 nm. This observation is consistent with the hexagonal P3m1 crystal structure that is suggested by the SAED pattern (figure 2(f)) [27]. A schematic of the P3m1 crystal structure in figure 2(a) is overlaid on the image for clarity. The blue and yellow spheres represent Cu and Te atoms, respectively.

HRSTEM-HAADF and bright field (BF) images of a thicker region on the same crystal are shown in figures 2(b) and (c). As copper telluride often possesses high concentrations of copper vacancies [5, 7], it is possible that non-uniformities can be detected at the nanoscale. For example, the intensity of some copper columns at the center of the six bright spots is decreased in figure 2(b). Likewise, the intensity of some copper columns increases in the BF image of figure 2(c).

The appearance of these vacancies at thicker regions of the flake hints towards the growth mechanism of these crystals. In this vapor-liquid growth mechanism, the chalcogen vapors diffuse into and saturate the molten catalyst as discussed above. Diffusion of Te is higher compared to the self-diffusion of Cu, which may explain the relatively higher Te concentration on the top crystal layers in contact with the sapphire substrate, where growth occurs [29, 30]. This is corroborated by the cross-sectional Cu/Te alloy in figure S6 where the Cu concentration relatively decreases towards the top surface. The effect of the diffusion variation is amplified with more crystal layers. This may contribute to the noticeable copper deficiencies in figures 2(b) and (c), which are a projection of all the layers in the thicker regions of the flake.

In figure S7, we show that having excess Te eventually ceases to yield Cu₂Te, and the Raman signal attributed to Cu₂Te disappears. Despite these vacancies, the inplane crystal structure remains consistent. In fact, the position of the vacancies agrees well with the lowest energy two-Cu-vacancy model in the trigonal lattice calculated by Yu *et al* [16].

To gain further insights into the structure of Cu₂Te, we prepared a focused ion beam (FIB) sample cutting into the planes of stacking to visualize the cross-sectional view as shown in figure 2(g). This FIB sample is prepared by mechanically transferring Cu₂Te on sapphire onto a SiO₂ substrate. In the HAADF image, from top to the bottom is the SiO₂ substrate, Cu₂Te crystals, and carbon capping layer. Essentially, the capping layer is laid on the surface that is facing the Cu foil during the growth. The extra thickness of Cu relative to Te at the interface with amorphous carbon is therefore most likely from unreacted molten Cu at the Cu/W interface. Focusing on a region of the cross-section, regular white, grey, and dark bands are observed along the c-axis of the crystal as shown in figure 2(h). The white bands correspond to tellurium-rich regions, while the grey and dark bands appear to correspond to copper-rich regions with differences in shade arising from variations in atomic density and tellurium concentration.

Phonon mode signatures reflect both the material and its crystal system [31]. The challenge with Cu_2Te synthesis has yielded a wide discrepancy in reported vibrational signatures including those of Cu_xTe pellets [22] and sputtered nominal Cu_2Te , which is a combination of Cu_7Te_5 and $Cu_{2-x}Te$ phases [32]. Only recently have some studies reported the Raman signature of Cu_2Te nanoplates in its P3m1 phase [20]. Our Raman spectra obtained in figure 3(a) demonstrate distinct peaks at 75, 90, 105, 145, and 215 cm⁻¹, verifying the P3m1 phase of the grown crystals. The peak fittings and Raman maps showing homogeneity of the flakes are shown in figure S8.

Raman spectroscopy is also a powerful tool to study layer-dependence in 2D materials [33]. Here, flakes of 2, 5, 8, 10, and 15 nm, as well as a bulk crystal of approximately 300 nm in thickness, are identified and a correlative study is conducted as shown in figure 3(a). Before reaching a critical thickness, two sapphire substrate peaks can be observed at 150 and 415 cm⁻¹ and are marked with '*'. Although the peak positions remain consistent, interestingly, there are significant changes in some peak intensities as the flakes get thicker. Notably, the peak at \sim 105 cm⁻¹ becomes dominant for bulk crystals, while that at \sim 215 cm⁻¹ is almost suppressed. Comparing the ratios of \sim 90 cm⁻¹ to \sim 105 cm⁻¹ modes in figure 3(b), there appears to be a relationship between the relative intensity and thickness of Cu₂Te. The ratio linearly decreases for thicknesses between 2 and 15 nm before a further drop for bulk flakes.

Using sapphire to prevent Cu from dewetting during the growth is pivotal to acquire flakes that are a few nanometers thick as shown in the atomic force microscopy (AFM) image in figure 3(c). Not only does the sapphire act as a second substrate on which growth is promoted, but also peeling the sapphire from the copper after the reaction has cooled exfoliates thin flakes. XPS is used to determine the surface elemental composition of the grown crystals on both copper and sapphire. Figures 3(d) and (e) show the spectra of Cu 2p and Te 3d, respectively. The Cu spectra show two distinct peaks at 932 and 952 eV, corresponding to Cu 2p_{3/2} and Cu 2p_{1/2} binding energies, respectively. A shoulder at 934.6 eV (and 954.4 eV) of Cu arises from CuO 2p _{3/2} (and CuO $2p_{1/2}$) and hints at the presence of oxidation. For Te, peaks at 572.7 and 583.2 eV correspond to the Te $3d_{5/2}$ and Te_{3/2} binding energies, respectively. Small bumps at 576 and 586.3 eV, assigned to the Te⁴⁺ 3d binding energies, indicate oxidation in the form of TeO₂ [15]. Since the flakes are exposed to ambient conditions after peeling off the sapphire from W, there is a possibility of localized oxygen presence on the surface. To corroborate this, XPS depth profiling is conducted as shown in figure S9, which shows the removal of oxygen signal by 30 s of plasma exposure.

In order to minimize surface oxidation on the flake used for device fabrication, the grown Cu₂Te samples were kept in the glove box until ready for immediate use. Moreover, it is known that the conductivity of Cu₂Te depends significantly on Cu deficiencies [34]. Therefore, to avoid exposure to solvents and resists which can potentially react with the flakes, we fabricated the Cu₂Te devices using a dry shadow mask-based technique. Elemental composition is confirmed afterwards using secondary ion mass spectroscopy (SIMS) as shown in figure 4(a) and S11 [35]. Variable temperature charge transport measurements down to 6 K taken in an inert environment are shown in figure S12. The extracted resistance shown in figure 4(b) clearly indicates a non-linear resistance-temperature relationship. At room temperature, the device shows a conductivity of $\sim 3 \times 10^3$ S cm⁻¹ (flake thickness is 250 nm). At low temperatures, three distinct regions are observed suggesting a phase transformation. The resistance decreases with decreasing temperature from 300 K to \sim 200 K (region I) and from \sim 100 K to 6 K (region III). In contrast, the resistance increases with decreasing temperature from \sim 200 K to \sim 100 K (region II).

Regions I and III demonstrate metallic behavior while region II demonstrates semiconducting behavior. Band structure calculations are performed using DFT to further corroborate the metallic nature at room temperature. Figure 4(c) shows the electronic structure in the vicinity of the Fermi energy for the P3m1 monolayer Cu_2Te , which indicates a metallic nature. The band structure

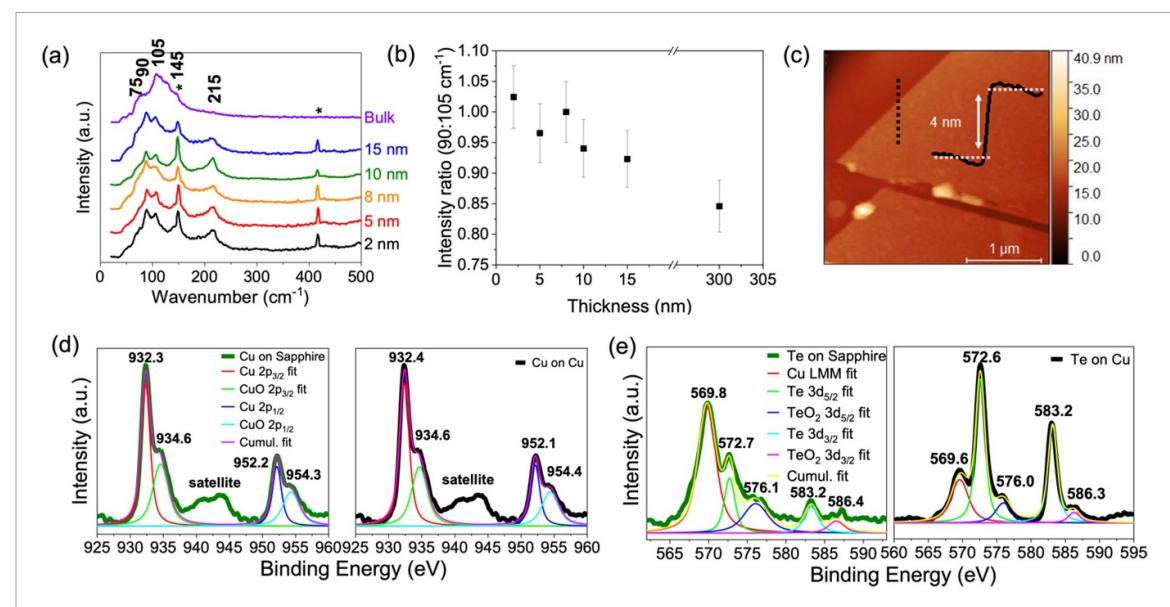


Figure 3. Structural analysis of grown Cu_2Te : (a) Raman spectra of as-grown Cu_2Te on sapphire at various thicknesses. (b) Ratio of \sim 90 cm⁻¹ and \sim 105 cm⁻¹ phonon modes as extracted from (a) illustrates that the ratio can be used to determine flake thicknesses. (c) AFM image of a clean, exfoliated Cu_2Te on sapphire with inset showing line profile of 4 nm thickness. XPS spectra of Cu_2Te on sapphire and copper show the presence of (d) copper and (e) tellurium and surface oxidation.

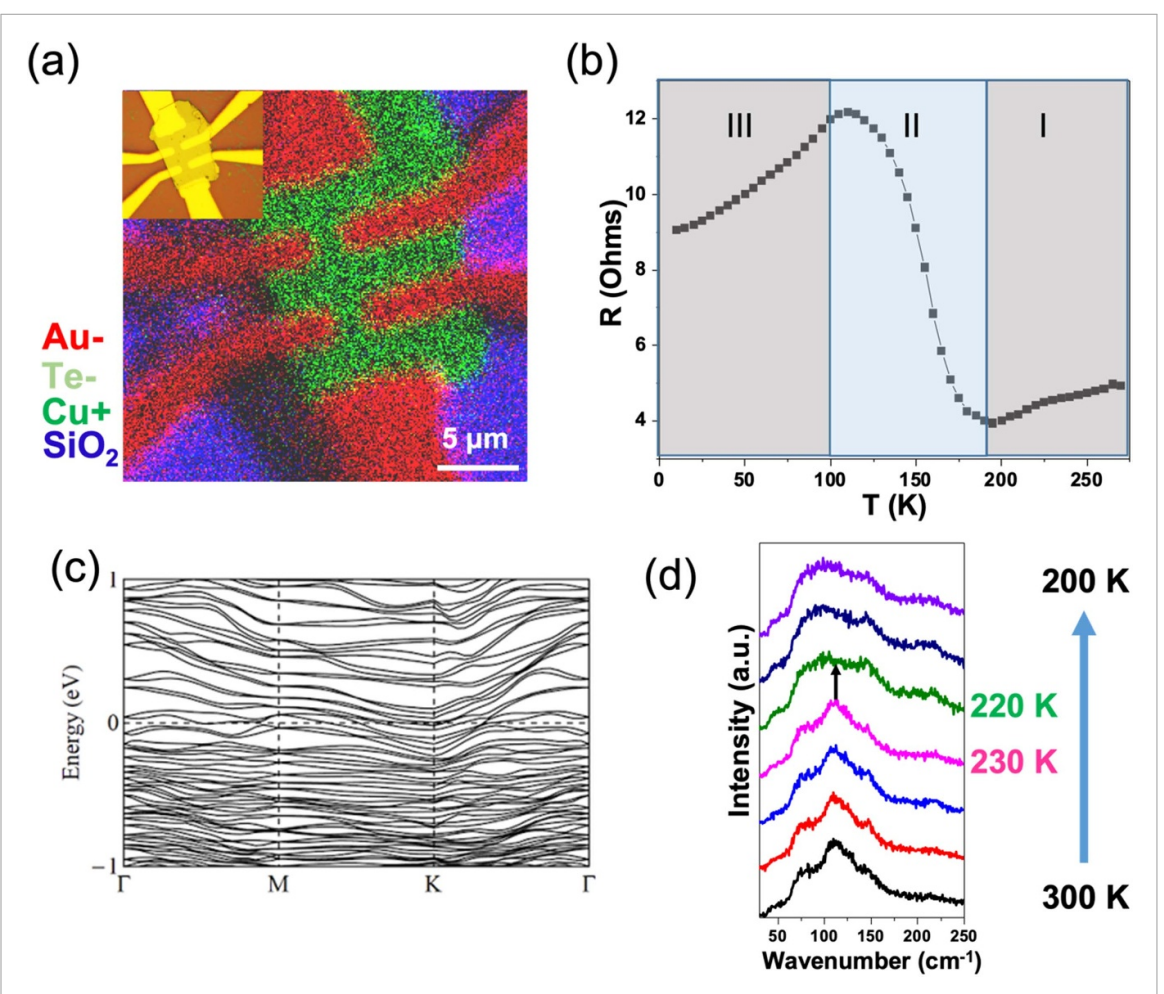


Figure 4. Low temperature transport properties of Cu_2 Te: SIMS elemental map after device fabrication is shown in (a). Inset shows the optical image of the transferred flake with Au contacts. Temperature-dependent resistance in (b) shows three different regions where Cu_2 Te transforms from the metallic phase to the semiconducting phase. Band structure of the P3m1 metallic phase is shown in (c). Low temperature Raman confirms the presence of a phase transition in (d).

is also calculated for different layers of Cu₂S (figure S13). Layer dependence and phase transition in these 2D material systems thereby provide additional knobs for tuning the physical and electronic structure.

In order to further probe the properties of the low temperature semiconducting phase, we recorded the transfer characteristics of the device ($I_{\rm sd}$ vs $V_{\rm g}$) at 160 K. However, no gate-tunability was observed. The lack of gate tunability may originate from significant doping of Cu₂Te from Cu vacancies, where in fact Cu₂Te was previously identified as degenerate semiconductor [36]. Cu₂Te has recently shown a similar phase transition from the P3m1 phase to the P6/mmm at higher temperatures of 423 K, which we confirmed in figure S14 [20]. However, to the best of our knowledge, no transition at low temperatures has been reported.

In order to corroborate the low temperature transition, we conducted low temperature Raman spectroscopy to observe any accompanying structural transition. There is an evident structural transition occurring between 230 and 220 K as shown in figure 4(c). The spectra show the phonon mode peaks of the P3m1 phase from room temperature down to 230 K. Below 220 K, a broad peak spanning between ~ 80 and ~ 140 cm⁻¹ appears as multiple low wavenumber phonon modes merge [19]. There is another broad peak at \sim 175 cm⁻¹, which is absent in the P3m1 phase. No further changes in the Raman spectra are seen. Although there is a small discrepancy in the transition temperature measured by Raman and transport measurements, it is important to note that the transition temperature can be different depending on the shape, size, and thickness of the crystals.

3. Summary and conclusion

In summary, we reported a reliable growth procedure for synthesizing Cu_2X (X = Te, Se, S) crystal systems via vapor-liquid interface growth using a stack of Al₂O₃/Cu/W. It is observed that liquid copper plays a significant role in catalyzing the growth of these 2D material systems, while sapphire assists with lateral growth and exfoliation. Thickness dependent phonon signatures are reported as a convenient method to estimate Cu₂Te thickness. The crystal structure of Cu_2 Te is found to be P3m1, which shows room temperature metallic nature by both DFT calculations and variable temperature charge transport measurements. Interestingly, a transition to a semiconducting phase occurs at low temperatures before a return to the metallic phase at even lower temperatures. This work not only presents a robust growth mechanism for a single phase layered Cu₂Te, but also reveals an existing low temperature phase transition.

This transition can be leveraged for varying the electronic structure of Cu₂Te from semiconducting to metallic with applications beyond photovoltaics and thermoelectrics to sensors, energy storage devices, and nanoelectronics.

4. Experimental methods

4.1. CVD growth of Cu₂X

Double side polished Cu foil (Alfa Aesar, 99.5% purity, $\sim 10 \ \mu \text{m}$ thick) was cut into $5 \times 5 \ \text{mm}^2$ pieces and sandwiched between a W foil (Alfa Aesar, 99.99% purity, $\sim 100 \ \mu m$ thick) and a sapphire substrate with similar dimensions. The stack was then placed in an alumina boat in a fused quartz tube with an inner diameter of 22 mm. Tellurium (Te) powder (10–100 mg) was placed upstream 15 cm away from the Al₂O₃/Cu/W substrate to reach the vaporization temperature. Al₂O₃/Cu/W substrates were heated to 1090 °C in a horizontal tube furnace (Lindberg Blue M) under H₂ (10 sccm) and Ar (100 sccm) at the rate of 20 °C min⁻¹. The temperature was then dropped to 1080 °C in 3 min for growth. The growth time varied from 10 to 30 min to get different flake densities. After the reaction, the samples were cooled down to 600 °C at a slower rate under Ar and H₂ flow. Then, H₂ flow was turned off and samples were quickly removed from the furnace to ensure rapid cooling to room temperature. Similarly for the growth of other crystals, Te powder was replaced by S and Se to get Cu₂S and Cu₂Se, respectively.

4.2. Characterization

A Horiba LabRam Confocal Raman equipped with a HJY detector was used to collect Raman spectra of all samples in ambient conditions. A 473 nm laser with 1800 gr mm⁻¹ grating and 25% ND filter was used. It is important to note that the grown crystals are sensitive to laser power in that higher power may damage the surface. Low and high temperature Raman spectroscopy was performed using a Linkam liquid nitrogen-based setup. Consistent flow of nitrogen is used to control the temperature with a step size of 10 K. Argon flow is used to avoid any moisture on the surface at low temperatures.

A Thermo Scientific ESCALAB 250Xi XPS instrument was used to obtain XPS spectra at room temperature using a 500 μ m spot size with a monochromatic Al Ka source. The spectra were referenced to the carbon peak at 284.5 eV.

A Bruker ICON AFM system was used in tapping mode in air with a scan rate of 1 Hz.

Cross-sectional TEM samples were prepared using a dual beam FEI Helios Nanolab SEM/FIB with a Ga ion-source. Before FIB sample preparation, flakes of Cu₂Te on the sapphire substrate were transferred onto a Si/SiO₂ substrate (300 nm native oxide layer) by mechanical exfoliation with Nitto polyvinyl

chloride (PVC) tape and heated to 100 °C for 5 min. Prior to lift-out, 200 nm of C was deposited with the electron beam and then 1.5 μ m of C was deposited with the ion beam. Lift-out and thinning were carried out with the ion beam at 30 kV. The sample was cleaned with the ion beam first at 5 kV and then at 2 kV.

TEM samples were prepared by wetting the sapphire substrate with ethanol. Then a molybdenum TEM grid was used to gently swipe over the grown crystals on sapphire. HRSTEM and SAED patterns were obtained using a probe-corrected JEOL ARM200CF microscope operated at 200 kV along the out-of-plane direction (c-axis), which is parallel to the [0001]-zone axis. STEM probe convergence angle was set to 27.1 mrad and current of 40 μ A. BF and HAADF STEM images were collected using collection angles ranging from 0 to 60 mrad and 90–370 mrad, respectively, with 8 μ s dwell time.

SIMS measurements were performed using a dual beam IONTOF M6 to analyze the elemental concentration of grown crystals. Secondary ion measurements were performed using a liquid bismuth ion beam (Bi⁺). A cesium ion gun with an energy of 500 eV was used to detect anions.

For electrical measurements, Cu_2 Te flakes were transferred on Si/SiO_2 substrates (figure S14) and Au contacts were evaporated through a shadow mask. Variable temperature charge transport measurements were performed using a Lakeshore CRX-4 K cryoprobe in vacuum.

4.3. DFT

P3m1 structure: All first-principles calculations were based on DFT and were performed using the Quantum ESPRESSO software package [37, 38] The calculations utilized the generalized gradient approximations of Perdew-Burke-Ernzerhoff [39] with ultra-soft pseudopotentials [40]. Spin-orbit effects were included for all band structure calculations. Inclusion of Hubbard U was neglected in all calculations. A plane-wave cutoff of 50 Ry was used in all calculations. For bulk calculations, the primitive unit cell belongs to P3m1 and was sampled with a Monkhorst-Pack k-mesh of $5 \times 5 \times 2$. The primitive unit cell dimensions are a = b = 8.37 Å, c = 21.60 Å. Unless stated, all samples were relaxed prior to calculation of electronic structure. During relaxation, spin-orbit effects were neglected, and the primitive unit cell was sampled with a Monkhorst-Pack k-mesh of $2 \times 2 \times 1$.

Data availability statement

The data that support the findings of this study are available from the corresponding author upon reasonable request.

Acknowledgments

This work was supported by NSF Division of Material Research (NSF Grant DMR-1929356-Program Manager: Lynnette Madsen). This work made use of the KECK II, EPIC, and SPID facilities of Northwestern University's NUANCE Center, which has received support from the SHyNE Resource [National Science Foundation (NSF) Grant ECCS-2025633], Northwestern's MRSEC program (NSF Grant DMR-1720139), the Keck Foundation, and the State of Illinois through IIN. The materials synthesis in this work was partially supported by the Army Research Office (Grant W911NF1910335). M C acknowledges support from the NSF Graduate Research Fellowship under Grant DGE-1842165. A T and P G were supported by the National Science Foundation MRSEC program (DMR-1720139) at the Materials Research Center of Northwestern University. D L acknowledges support from the Swiss National Science Foundation for an Early PostDoc Mobility Fellowship (P2EZP2_181614) in addition to the National Science Foundation Division of Materials Research (NSF DMR-2004420).

Supporting information

The following files are available free of charge.

Supplementary information on parameters controlling Cu₂X growths, elemental and vibrational modes, band structure calculations, and electrical measurements.

Author contribution

The manuscript was written through contributions of all authors. All authors have given approval to the final version of the manuscript.

ORCID iDs

Yea-Shine Lee https://orcid.org/0000-0002-2087-4886

Dmitry Lebedev https://orcid.org/0000-0002-1866-9234

Mark C Hersam https://orcid.org/0000-0003-4120-1426

Xinqi Chen https://orcid.org/0000-0003-0413-4893

References

- [1] Kang K, Xie S, Huang L, Han Y, Huang P Y, Mak K F, Kim C-J, Muller D and Park J 2015 High-mobility three-atom-thick semiconducting films with wafer-scale homogeneity Nature 520 656–60
- [2] Shi Y, Li H and Li L-J 2015 Recent advances in controlled synthesis of two-dimensional transition metal

- dichalcogenides via vapour deposition techniques *Chem.* Soc. Rev. 44 2744–56
- [3] Li S et al 2018 Vapour-liquid-solid growth of monolayer MoS₂ nanoribbons Nat. Mater. 17 535–42
- [4] van der Zande A M, Huang P Y, Chenet D A, Berkelbach T C, You Y, Lee G-H, Heinz T F, Reichman D R, Muller D A and Hone J C 2013 Grains and grain boundaries in highly crystalline monolayer molybdenum disulphide Nat. Mater. 12 554–61
- [5] Geng D, Wu B, Guo Y, Huang L, Xue Y, Chen J, Yu G, Jiang L, Hu W and Liu Y 2012 Uniform hexagonal graphene flakes and films grown on liquid copper surface *Proc. Natl Acad.* Sci. 109 7992–6
- [6] Xu C, Wang L, Liu Z, Chen L, Guo J, Kang N, Ma X-L, Cheng H-M and Ren W 2015 Large-area high-quality 2D ultrathin Mo₂C superconducting crystals *Nat. Mater.* 14 1135–41
- [7] Hong Y-L et al 2020 Chemical vapor deposition of layered two-dimensional MoSi₂N₄ materials Science 369 670–4
- [8] Shehzad M A, Das P M, Tyner A C, Cheng M, Lee Y-S, Goswami P, Reis R D, Chen X and Dravid V P 2022 Synthesis of layered vs planar Mo₂C: role of Mo diffusion 2D Mater. 9 015039
- [9] Trentler T J, Hickman K M, Goel S C, Viano A M, Gibbons P C and Buhro W E 1995 Solution-liquid-solid growth of crystalline iii–V semiconductors: an analogy to vapor-liquid-solid growth *Science* 270 1791–4
- [10] Zavabeti A et al 2017 Reaction environment for the room-temperature synthesis of atomically thin metal oxides Science 358 332–5
- [11] Chen J et al 2017 Chemical vapor deposition of large-size monolayer MoSe₂ crystals on molten glass J. Am. Chem. Soc. 139 1073–6
- [12] Gao L, Zhang Y-F and Du S 2021 Semiconducting M₂X (M = Cu, Ag, Au; X = S, Se, Te) monolayers: a broad range of band gaps and high carrier mobilities *Nano Res*. 14 2826–30
- [13] He Y, Zhang T, Shi X, Wei S-H and Chen L 2015 High thermoelectric performance in copper telluride NPG Asia Mater. 7 e210
- [14] Mallick M and Vitta S 2017 Realizing high figure-of-merit in Cu2Te using a combination of doping, hierarchical structure, and simple processing J. Appl. Phys. 122 024903
- [15] Park D, Ju H, Oh T and Kim J 2018 Facile fabrication of one-dimensional Te/Cu₂Te nanorod composites with improved thermoelectric power factor and low thermal conductivity Sci. Rep. 8 18082
- [16] Yu L, Luo K, Chen S and Duan C-G 2015 Cu-deficiency induced structural transition of Cu_{2-x}Te CrystEngComm 17 2878–85
- [17] Feng J, Gao H, Li T, Tan X, Xu P, Li M, He L and Ma D 2021 Lattice-matched metal–semiconductor heterointerface in monolayer Cu₂Te ACS Nano 15 3415–22
- [18] Pandey J, Mukherjee S, Rawat D, Athar S, Rana K S, Mallik R C and Soni A 2020 Raman spectroscopy study of phonon liquid electron crystal in copper deficient superionic thermoelectric Cu_{2-x}Te ACS Appl. Energy Mater. 3 2175–81
- [19] Zhang Y, Sa B, Zhou J and Sun Z 2014 First principles investigation of the structure and electronic properties of Cu₂Te Comput. Mater. Sci. 81 163–9
- [20] Zhang Y, Zhang Z, Liu W, Zheng Y, Wu Y, Su J, Liu N and Gao Y 2021 *In Situ* insight into thermally-induced reversible

- transitions of crystal structure and photoluminescence properties in Cu₂Te nanoplate *J. Mater. Chem.* A 9 26095–104
- [21] Ballikaya S, Chi H, Salvador J R and Uher C 2013 Thermoelectric properties of Ag-doped Cu₂Se and Cu2Te J. Mater. Chem. A 1 12478–84
- [22] Qian K et al 2019 Epitaxial growth and air-stability of monolayer Cu₂Te Chin. Phys. B 29 018104
- [23] Tong Y et al 2020 Evidence of new 2D material: $Cu_2Te\ 2D$ Mater. 7 035010
- [24] Siddique S *et al* 2021 Emerging two-dimensional tellurides *Mater. Today* **51** 402–26
- [25] Inagaki N, Ejima T and Kameda M 1965 Inter-diffusion coefficients of sulfur, selenium, and tellurium in liquid copper J. Miner. Metall. Inst. Japan 81 1045–52
- [26] Xie S et al 2016 A high-quality round-shaped monolayer MoS₂ domain and its transformation Nanoscale 8 219–25
- [27] Lesyuk R, Klein E, Yaremchuk I and Klinke C 2018 Copper sulfide nanosheets with shape-tunable plasmonic properties in the NIR region *Nanoscale* 10 20640–51
- [28] Pollmann E, Maas A, Marnold D, Hucht A, Neubieser R-M, Stief M, Madauß L and Schleberger M 2022 Dynamic growth/etching model for the synthesis of two-dimensional transition metal dichalcogenides via chemical vapour deposition 2D Mater. 9 035001
- [29] Kuper A, Letaw H, Slifkin L, Sonder E and Tomizuka C T 1954 Self-diffusion in copper Phys. Rev. 96 1224–5
- [30] Ghoshtagore R N 1967 Self-Diffusion in tellurium. I. Anisotropy and impurity effect *Phys. Rev.* 155 598–602
- [31] Pizzi G, Milana S, Ferrari A C, Marzari N and Gibertini M 2021 Shear and breathing modes of layered materials ACS Nano 15 12509–34
- [32] Salmón-Gamboa J U, Barajas-Aguilar A H, Ruiz-Ortega L I, Garay-Tapia A M and Jiménez-Sandoval S J 2018 Vibrational and electrical properties of Cu_{2-x}Te films: experimental data and first principle calculations Sci. Rep. 8 8093
- [33] Liang L and Meunier V 2014 First-principles Raman spectra of MoS₂, WS₂ and their heterostructures *Nanoscale* 6 5394
- [34] Li B, Huang L, Zhao G, Wei Z, Dong H, Hu W, Wang L-W and Li J 2016 Large-size 2D β -Cu₂S nanosheets with giant phase transition temperature lowering (120 K) synthesized by a novel method of super-cooling chemical-vapor-deposition *Adv. Mater.* **28** 8271–6
- [35] Tien D H, Park J-Y, Kim K B, Lee N and Seo Y 2016 Characterization of graphene-based FET fabricated using a shadow mask Sci. Rep. 6 25050
- [36] Qiu Y, Liu Y, Ye J, Li J and Lian L 2018 Synergistic optimization of carrier transport and thermal conductivity in Sn-doped Cu₂Te J. Mater. Chem. A 6 18928–37
- [37] Kresse G and Furthmüller J 1996 Efficient iterative schemes for ab initio total-energy calculations using a plane-wave basis set *Phys. Rev.* B 54 11169–86
- [38] Giannozzi Pet al 2020 Quantum ESPRESSO toward the exascale J. Chem. Phys. 152 154105
- [39] Perdew J P, Burke K and Ernzerhof M 1996 Generalized gradient approximation made simple *Phys. Rev. Lett.* 77 3865–8
- [40] Kresse G and Joubert D 1999 From ultrasoft pseudopotentials to the projector augmented-wave method Phys. Rev. 59 1758